

# Wave-Breaking Turbulence in the Ocean Surface Layer

JIM THOMSON, MICHAEL S. SCHWENDEMAN, AND SETH F. ZIPPEL

*Applied Physics Laboratory, University of Washington, Seattle, Washington*

SAEED MOGHIMI

*Oregon State University, Corvallis, Oregon*

JOHANNES GEMMRICH

*University of Victoria, Victoria, British Columbia, Canada*

W. ERICK ROGERS

*Naval Research Laboratory, Stennis Space Center, Louisiana*

(Manuscript received 12 July 2015, in final form 17 March 2016)

## ABSTRACT

Observations of winds, waves, and turbulence at the ocean surface are compared with several analytic formulations and a numerical model for the input of turbulent kinetic energy by wave breaking and the subsequent dissipation. The observations are generally consistent with all of the formulations, although some differences are notable at winds greater than  $15 \text{ m s}^{-1}$ . The depth dependence of the turbulent dissipation rate beneath the waves is fit to a decay scale, which is sensitive to the choice of vertical reference frame. In the surface-following reference frame, the strongest turbulence is isolated within a shallow region of depths much less than one significant wave height. In a fixed reference frame, the strong turbulence penetrates to depths that are at least half of the significant wave height. This occurs because the turbulence of individual breakers persists longer than the dominant period of the waves and thus the strong surface turbulence is carried from crest to trough with the wave orbital motion.

## 1. Introduction

Wave breaking at the ocean surface limits wave growth (Melville 1994), enhances gas exchange (Zappa et al. 2007), and generates turbulence that mixes the ocean surface layer (Burchard et al. 2008; Kukulka and Brunner 2015). Previous observations of wave-breaking turbulence have shown strong enhancement near the surface, at values that far exceed those predicted by simple “law of the wall” boundary layer scaling (Agrawal et al. 1992; Terray et al. 1996;

Gemmrich and Farmer 2004; Gemmrich 2010). The dynamic balance assumed is that the wave energy lost during breaking  $S_{\text{brk}}$  becomes a flux of turbulent kinetic energy  $F$  into the ocean surface layer that is dissipated at a rate  $\varepsilon(z)$ , which varies with depth  $z$  beneath the surface:

$$\int S_{\text{brk}} df \approx F \approx \int \varepsilon(z) dz. \quad (1)$$

Here, the wave energy loss is integrated over a range of frequencies  $f$ , and the vertical reference frame for depth  $z$  can either be wave following, noted as  $z_w$ , or fixed, noted as  $z$ . On average, the wave-following surface must, by definition, become the mean sea level, such that  $\langle z_w = 0 \rangle \rightarrow z = 0$ . However, the wave-resolved  $\varepsilon$  may not be symmetric, such that the average  $\varepsilon$  is likely different between the two reference frames. Reconciling these reference frames is essential to comparing the

 Denotes Open Access content.

Corresponding author address: Jim Thomson, Applied Physics Laboratory, University of Washington, 1013 NE 40th St., Seattle, WA 98105.  
E-mail: jthomson@apl.washington.edu

DOI: 10.1175/JPO-D-15-0130.1

different observations of  $\varepsilon$  reported in the literature, and it also is essential to obtaining a consistent total energy dissipation rate when depth integrating  $\int \varepsilon(z) dz$ . This simple balance neglects transport of turbulence and buoyancy work by bubbles, both of which may be significant in strongly forced conditions.

Formulations for the total energy flux  $F$  typically begin with the momentum flux from a wind stress  $\tau = \rho_a u_{*a}^2$  because wave breaking in deep water (i.e., whitecaps) is dominated by the short, wind-driven waves. Here,  $u_{*a}$  is the air-side friction velocity, which we convert to a water-side friction velocity  $u_{*w} = (\rho_a/\rho_w)^{1/2} u_{*a}$ , using the ratio of the air and water densities. Dropping the subscript  $w$ , the water-side  $u_*$  is used throughout the formulations that follow. The wind stress acts upon the waves, which are roughness elements at the free surface, and thus some formulations for total energy flux include the speeds or scales of the waves in prescribing the work done by the wind stress. The subsequent dissipation of energy happens in a region of depth  $z$  where waves are a dominant process, which is a working definition of the ocean surface layer in any of the respective vertical reference frames.

One common scaling for turbulence in the ocean surface layer is based on the shear production of an applied stress acting on a surface with a characteristic speed (e.g., [Craig and Banner 1994](#)). In this approach, the input of turbulent kinetic energy (TKE) increases with the cube of the friction velocity

$$F_1 = \alpha u_*^3, \quad (2)$$

where  $\alpha$  is a constant, typically  $O(10^2)$ . Although the actual values exceed the log-layer estimates, the physical scaling for the TKE input is a generic boundary layer scaling because the additional velocity scale multiplied with  $\tau$  is  $u_*$  (as opposed to a velocity scale associated with the waves). [Craig and Banner \(1994\)](#) apply this  $u_*^3$  input in a diffusive model for the vertical structure of the turbulent dissipation rate  $\varepsilon(z)$ , which is now in regular usage (e.g., [Gerbi et al. 2013](#)).

Turbulence generation during wave breaking, however, creates a boundary layer that may not scale as simply as the cube of the friction velocity. Wave breaking is an intermittent process that injects turbulence at scales related to the waves themselves, rather than the wind alone. Recognizing the importance of wave scales, [Gemmrich et al. \(1994\)](#) proposed a different form for the TKE input, which uses an effective speed  $c_e$  to transfer the wind stress  $\tau$  into the surface as TKE, such that

$$F_2 = c_e \tau = c_e u_*^2. \quad (3)$$

[Gemmrich et al. \(1994\)](#) relate  $c_e$  to short waves that dominate the roughness of the ocean surface and find that  $c_e \sim 1 \text{ m s}^{-1}$ . This is a bulk value that is meant to represent the range wave speeds that carry the stress from the wind. Although the correct  $c_e$  is still an open question, the important aspect of this formulation is that the wind stress  $\tau = \rho_a u_*^2$  is imparted to the waves, as represented by  $c_e$ , not just a mean sheared current, which would be represented by another factor of  $u_*$  [as in Eq. (2)]. Conceptually,  $c_e$  should be related to the speed of the roughness elements (i.e., the short waves).

Although it has not been adopted in the subsequent literature, [Phillips \(1985\)](#) also considered an adjustment to the energy fluxes based on wave scales. [Phillips \(1985, p. 522\)](#) wrote, “the energy source for near-surface turbulence represented by wave breaking is, in mean, distributed over a wide range of scales, rather than being concentrated at the energy-containing scales as it is in shear-generated turbulence.” His formulation considers the available flux, defined as  $u_*^3$ , that can be carried by wavenumbers bounding the “equilibrium range”  $k_0$  and  $k_1$ . The result is a formulation for a balance of total dissipation and total TKE input given by

$$F_3 = 2\gamma\beta^3 I(3p) u_*^3 \ln\left(\frac{k_1}{k_0}\right), \quad (4)$$

where the combined constants  $\gamma\beta^3 I(3p)$  are approximately  $10^{-3}$ . The wavenumber limits are defined by a lower bound that is twice the peak wavenumber  $k_0 = 2k_p$  and an upper bound that is caused by suppression of waves that are slower than the drift speed of the surface, which can be related to the wind friction velocity by  $k_1 = g/u_*^2$ . In practice, the factor  $\ln(k_1/k_0)$  in Eq. (4) limits the increase in energy flux at high winds by narrowing the range of scales on which the wind acts. A wave spectrum with a smaller equilibrium range will have a smaller ratio of  $k_1/k_0$  and thus a smaller input rate  $F_3$ . This dependence on the short waves is loosely similar to using an effective speed that remains tied to short (and relatively slow) waves in Eq. (3).

[Phillips \(1985\)](#) argued that these wavenumbers were the scales in which wave-breaking dissipation was in balance with wind input and nonlinear transfers within the spectrum, hence the term equilibrium range. Equilibrium also was proposed by [Kitaigorodskii \(1983\)](#), although with a different derivation. The equilibrium hypothesis has been shown to be consistent with wave-breaking turbulence measurements under moderate wind speeds ([Thomson et al. 2013](#)). Assuming equilibrium, and using a wind input formulation from [Plant \(1982\)](#), the TKE input is

$$F_4 = \int S_{\text{wind}} df = \int \frac{u_*^2}{c^2} \cos(\theta) (2\pi f) E(f) df, \quad (5)$$

where  $\theta$  is the relative difference between the wind and wave direction at every frequency  $f$  of the wave energy spectrum  $E$ , and the factor of 0.04 in Plant (1982) is omitted because the adjustment of  $(\rho_a/\rho_w)^{1/2}$  has already been made in determining the water-side  $u_*$ . In deep water, the phase speed is  $c = g/(2\pi f)$ , and thus the net dependence of  $S_{\text{wind}}$  weights the high frequencies with  $f^3$ . This is similar in character to the  $f^4$  weighting of the mean square slope and the  $f^5$  weighting of the “wave saturation” (Banner et al. 2002; Hwang et al. 2012), both of which have been correlated with wave-breaking turbulence (Gemmrich 2010).

Finally, dissipation is calculated using a formulation in the WAVEWATCH III spectral wave model (Tolman 1991; Tolman and Chalikov 1996; Tolman et al. 2014). The spectral dissipation from the wave model, integrated over equilibrium range frequencies, can be used as yet another estimate of the TKE input:

$$F_5 = \int S_{\text{brk}} df, \quad (6)$$

which is applied at the ocean surface wave via breaking.

In addition to the total energy flux and equilibrium balance of breaking waves, the depth dependence of this balance has been presented in several previous papers. For example, Terray et al. (1996) apply the model for vertical diffusion of the TKE input from Craig and Banner (1994) and assess  $F_1$  and  $F_2$  using observations of small whitecaps on Lake Ontario. Terray et al. (1996) evaluate the scaling

$$\left( \frac{\varepsilon H_s}{F} \right) \propto \left( \frac{z}{H_s} \right)^{-\lambda}, \quad (7)$$

where  $z$  is the fixed depth beneath the mean water level,  $\lambda$  is the exponential decay rate, and  $H_s$  is the significant wave height. Their data were collected in conditions of 7 to 16 m s<sup>-1</sup> winds and 0.2- to 0.5-m significant wave heights. In terms of depth dependence, they proposed three distinct vertical regions in a fixed reference frame: 1) a breaking zone,  $0 < z/H_s < 0.6$ , which has half of the total dissipation and a constant profile; 2) a transition layer, which follows  $(z/H_s)^{-2}$  and depends on wave age; and 3) a deep logarithmic layer  $\ln(z)$ . They did not make measurements in region 1 but rather inferred this using the dissipation necessary to meet the equilibrium assumption.

More recently, Gemmrich (2010) presented measurements in a wave-following reference frame  $z_w$  and found the largest dissipation rates to occur exclusively in

the wave crests, above the still water level. He fit the vertical decay of the turbulence using Eq. (7) and obtained  $-1.5 < \lambda < -1$ , with a deep log layer below one  $H_s$ . Similarly, wave tank measurements of spilling waves on a sloping beach suggest that 80% of the total dissipation occurs above the still water level (Govender et al. 2004). Gemmrich (2010) converted the wave-following measurements to a fixed vertical coordinate, which resulted in maximum dissipation at  $z \approx 0.3H_s$ . Since the adjusted reference frame produces an apparent decrease in the near-surface dissipation, Gemmrich (2010) noted the reference frame conversion as a severe limitation for representing wave-breaking turbulence in numerical models that use a flat surface. The Gemmrich (2010) results are scaled by wind stress [Eq. (2)] in conditions that range from 0 to 15 m s<sup>-1</sup> winds, with fetch-limited waves that are less than  $H_s < 0.5$  m. Recently, Sutherland and Melville (2015) used similar methods and found that  $\lambda \sim 1$  near the surface (within one wave height) and  $\lambda \sim 2$  below that [Eq. (7)].

This paper uses a comprehensive dataset to evaluate existing formulations for wave-breaking turbulence. Data are from the vicinity of Ocean Weather Station P (OWS-P) in the North Pacific (50°N, 145°W), and this work extends the results of a previous study at that site with lower winds (Thomson et al. 2013). The previous study analyzed wave equilibrium but did not scale the surface turbulence nor address the reference frames. Here, the emphasis is scaling the surface turbulence in a new dataset that extends to 20 m s<sup>-1</sup> winds and reconciling the wave-following reference frame of the observations with the fixed reference frame of the models. Section 2 describes the data collection and processing methods. Section 3 presents the results. Section 4 discusses the implications. Section 5 concludes.

## 2. Methods

### a. Observations

Wave, wind, and surface turbulence data were collected in the vicinity of OWS-P at 50°N, 145°W. The data were collected during a mooring turnaround cruise in January 2015 aboard the R/V *Thomas G. Thompson*. Several surface wave instrument floats with tracking (SWIFTs; see Thomson 2012) were deployed to measure profiles of the near-surface turbulence dissipation rate. A three-axis sonic anemometer (RM Young model 8100) was mounted to the jackstaff at the bow of the ship to measure turbulent winds at 16-m height above the surface. Wave spectral measurements were collected from the SWIFTs as well as a 0.9-m Datawell directional waverider (DWR MKIII) moored at OWS-P. Video

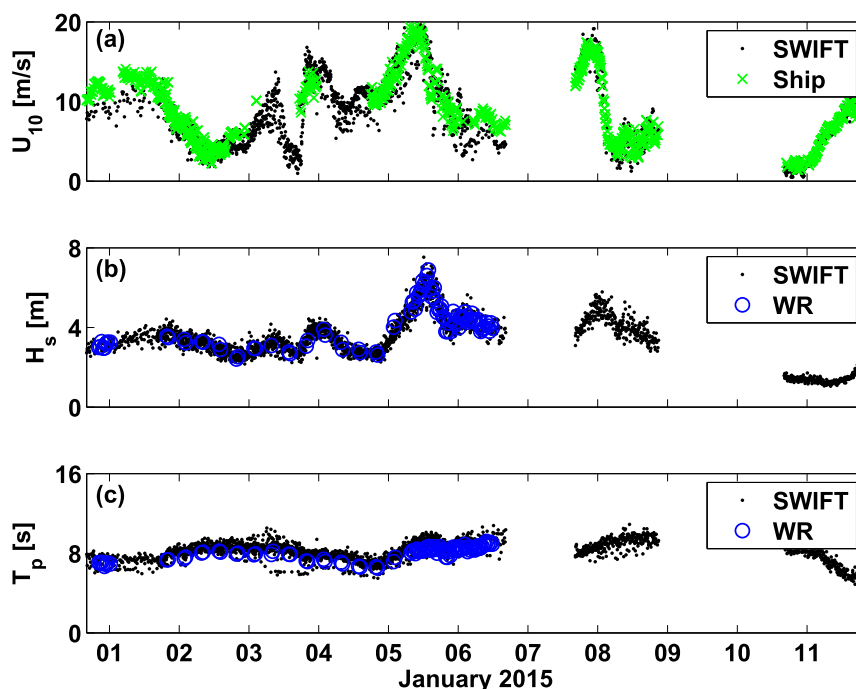


FIG. 1. Range of conditions observed. (a) Wind speeds, (b) significant wave heights, and (c) peak wave periods. Black points are from SWIFTs, green crosses are from the shipboard sonic anemometer, and blue circles are from the waverider.

measurements of wave breaking were also collected and are reported in a separate paper, along with a more detailed analysis of the wave spectra (Schwendeman and Thomson 2015).

Figure 1 shows the wind and wave conditions during the cruise. The waves were predominantly pure seas, which evolved during the storms. There was a limited amount of swell from remote sources. Wave conditions are shown from both the SWIFTs and waverider; however, the waverider values are only shown when the SWIFTs and the ship were within 30 nautical miles of the waverider. Using a 10-min burst length for ensemble estimation, the full dataset is composed of 2522 observations.

#### b. Wind stress estimates $u_{*a}$

The sonic anemometer data from the jackstaff of the ship were processed according to the inertial dissipation method of Yelland et al. (1994), in which an air-side dissipation rate is estimated from turbulence spectra and then used to infer the wind friction velocity  $u_{*a}$ . The sonic anemometer data were collected at 10 Hz and parsed into 128-point windows that were despiked following Goring and Nikora (2002); then they were tapered and overlapped 50% and finally fast Fourier transformed. Ensemble spectra were made at 10-min intervals by averaging 46 subwindows to obtain final

spectra with 0.0391-Hz frequency resolution and 92 degrees of freedom.

The ensemble spectra were fit to an expected frequency dependence of  $f^{-5/3}$  in the inertial frequency subrange ( $1 < f < 4$  Hz), and the air-side friction velocity was estimated assuming advection of a frozen field (Taylor's hypothesis) at a speed  $U$ , such that

$$u_{*a} = \left\{ \kappa \left[ \frac{\langle E_a(f) f^{5/3} \rangle}{K \left( \frac{U}{2\pi} \right)^{2/3}} \right]^{3/2} z_a \right\}^{1/3}, \quad (8)$$

where  $K = 0.55$  is the horizontal Kolmogorov constant,  $\kappa = 0.4$  is the von Kármán constant, and  $z_a = 16$  m is the measurement height above the still water level. This assumes neutral stability, which is justified by the similarity of water and air temperatures during the observations (typically within 2°C). The resulting estimates of wind stress  $\tau = \rho_a u_{*a}^2$  are typically within 10% of estimates generated using standard drag coefficients in  $\tau = \rho_a C_D U_{10}^2$  (Smith 1988).

The wind stress estimates from the ship are expanded using the wind speed measurements from the SWIFTs and standard drag coefficients, which are applied after adjusting the SWIFT winds from  $z_a = 1$  m measurement height to the  $z_a = 10$  m standard. The air-side friction

velocities are converted to water-side friction velocities  $u_* = (\rho_a/\rho_w)^{1/2} u_{*a}$ , using the ratio of the air and water densities.

### c. WAVEWATCH III model runs

The numerical wave model used here is WAVEWATCH III (Tolman 1991; Tolman et al. 2014), with the physics package of Ardhuin et al. (2010). The geographic grid is global, at  $0.5^\circ$  resolution, and the spectral grid includes 36 directional bins and 31 frequency bins (0.0418 to 0.72 Hz, logarithmically spaced). An obstruction grid is used to represent unresolved islands (Tolman et al. 2014). Winds and ice concentrations are taken from the Navy Global Environmental Model (NAVGEN; Hogan et al. 2014), with the former input at 3-h intervals and the latter at 12-h intervals. The simulation is initialized 0000 UTC 1 December 2014 and ends 0000 UTC 1 February 2015. The required spinup time, during which predictions of remote swells are invalid, is estimated to end 0000 UTC 15 December 2014. The physics package of Ardhuin et al. (2010) requires specification of a parameter  $\beta_{\max}$ , which is used to compensate for the mean bias of the input wind fields or lack thereof;  $\beta_{\max} = 1.2$  is used for this hindcast. The model version number employed is development version 5.08. In context of the present application, this is not substantially different from public release version 4.18.

### d. Wave displacement estimates

The SWIFTs collected GPS velocities of 4 Hz on a 12-min duty cycle, in which data were collected for a 512-s burst and then processed on board the buoy and transmitted in the remaining 208 s before resuming data collection. Wave energy spectra  $E(f)$  were estimated following the methods of Herbers et al. (2012). The waverider collected buoy pitch, roll, and heave displacements at 1.28 Hz on a 30-min duty cycle, following the Datawell standards. Both types of buoys processed data on board at the end of each duty cycle and transmitted the spectral moments to servers on shore via Iridium satellites.

In addition to the GPS receivers, the SWIFT buoys were equipped with MicroStrain 3DM-GX3-35 sensors, which measure three axes of acceleration, rotation rate, and orientation at 25 Hz. These measurements were used to define the quaternion orientation matrix at 25 Hz, from which true vertical heave accelerations (in the earth reference frame) were calculated. These accelerations were integrated twice in the time domain, with a high-pass filter at each integration, to reconstruct a wave-resolved time series of sea surface elevations  $\eta$ , relative to mean sea level. The elevations were used to calculate wave energy spectra, and these are compared

with the energy spectra from the GPS velocity method of Herbers et al. (2012) and with the output of the Datawell waverider. Agreement is within 5% for most cases. These elevations were down sampled to 0.5 Hz and used to map turbulence measurements, collected in the wave-following reference frame of the buoy  $z_w$ , to a fixed reference frame  $z$ .

### e. Turbulent dissipation rate estimates $\varepsilon$

The SWIFTs collected pulse-coherent Doppler sonar (Nortek Aquadopp HR) profiles of turbulent velocities beneath the wave-following surface denoted as  $z_w = 0$ . The details of data collection, quality control, and processing are described in Thomson (2012) and will only be reviewed here. The primary differences here are to use the double-sided structure function (i.e., velocity variations above and below each bin) and to calculate wave-resolved estimates before creating burst-averaged ensemble values. The wave-resolved estimates are necessary to directly map the measurements from a wave-following reference frame to a fixed reference frame.

The turbulent velocities were collected at 4 Hz and were processed to estimate the second-order structure function of the turbulent velocity fluctuations beneath the wave-following surface at 2-s intervals ( $=0.5$  Hz) after application of pulse correlation quality control (minimum correlation of 30). The structure function is a direct spatial realization of the theoretical Kolmogorov (1941) energy cascade from large to small scales. Fitting the observed structure function  $D(z_w, r) \sim r^{2/3}$ , where  $r$  is the spatial separation of velocity measurements along a profile, is equivalent to fitting a  $k^{-5/3}$  wavenumber spectrum, and thus the turbulent dissipation rates were estimated according to Wiles et al. (2006):

$$\varepsilon(z_w) = \left[ \frac{C_v^2}{A(z_w)} \right]^{3/2}, \quad (9)$$

where  $C_v = 1.45$  is a constant, and  $A(z_w)$  is the amplitude of the structure function determined for each  $z_w$  from fitting  $D(z_w, r) = Ar^{2/3} - N$ . Here,  $N$  is the contribution to variance from noise in the Doppler measurements; it is a free parameter in the fit to  $r^{2/3}$  and is checked against the expected noise of the profiler (see Thomson 2012).

### f. Vertical reference frames

The wave-resolved values (2 s) are mapped to the fixed reference frame and used to calculate burst-averaged values (512 s). In the wave-following frame,  $z_w = 0$  is the instantaneous surface, and results go down to  $z_w = -0.5$  m. In the fixed reference frame,  $z = 0$  is the mean sea level, and  $\eta$  is the instantaneous wave surface



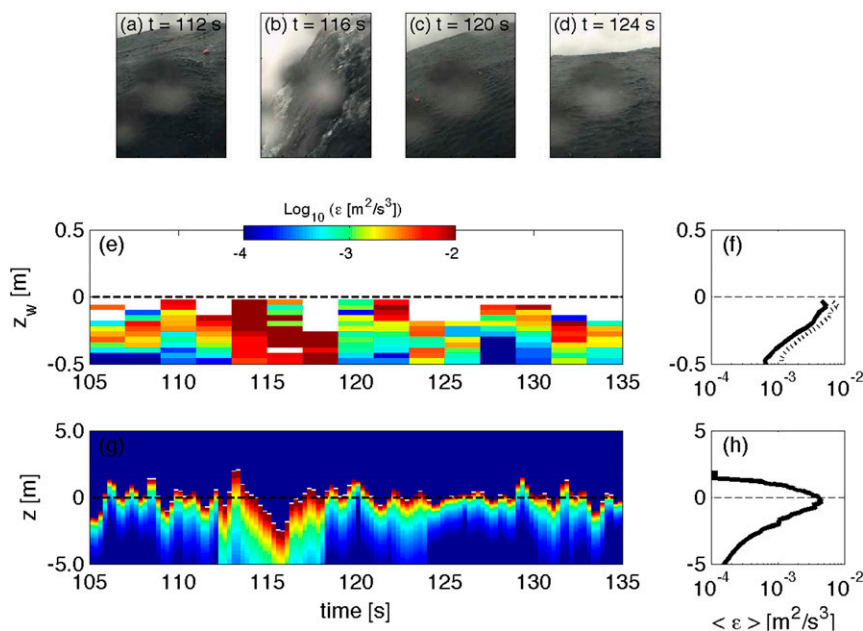


FIG. 2. (a)–(d) An example 30-s time series of a breaking wave, which is confirmed using images collected on board the SWIFT. The wave-resolved turbulent dissipation rate profiles are measured in a (e) wave-following reference frame that is directly mapped to a (g) fixed reference frame using the surface elevation time series. burst-averaged profiles, using 512 s of data, and (f), (h) shown for each reference frame. The fixed reference frame results include data extrapolation from the wave-following reference frame, such that all depths are averaged uniformly. The dashed line in (f) shows a burst-averaged dissipation rate profile calculated directly from all the velocities measured in the burst rather than taking the average of the wave-resolved profiles.

relative to mean sea level. The wave-resolved  $\varepsilon(z_w)$  values are mapped to  $\varepsilon(z)$  using  $z = \eta - z_w$ , where  $z$  is gridded at 0.1-m resolution. Both  $\varepsilon(z_w)$  and  $\varepsilon(z)$  are burst averaged over 512 s at each value of  $z_w$  or  $z$  to create  $\langle \varepsilon(z_w) \rangle$  and  $\langle \varepsilon(z) \rangle$ .

In mapping to the gridded  $z$  reference frame, only a subset of the grid cells is populated. To avoid biases caused by data sparsity when subsequently calculating burst-averaged profiles of dissipation in the fixed reference frame, the missing values are filled via extrapolation. The extrapolation is done in the wave-following reference frame before mapping to the fixed reference frame. The wave-resolved dissipation values above sea surface are assigned zero. The dissipation values below the deepest observation are extrapolated by fitting the power-law decay of Eq. (7) using a constant  $\lambda = 1.4$ , which is determined from a logarithmic fit to the entire dataset.

Figure 2 shows an example of the wave-resolved dissipation rates and the corresponding burst-averaged results in each reference frame. This particular example has a breaking wave at  $t = 113$  s, as indicated by the surface images collected on board the buoy every 4 s

(Figs. 2a–d). Note that only 30 s of data are shown in the wave-resolved panels, such that the individual breaker can be seen, but the burst-averaged panels show results calculated using the whole 512-s data burst. Other bursts are similar, including the shift of the very shallow  $\varepsilon(z_w)$  profiles to much greater depths in  $\varepsilon(z)$ . The shift occurs because the changing surface elevation  $\eta$  carries the  $z_w$  coordinates through several meters of  $z$ . Another similarity across the various bursts of data is the long time scale of  $\varepsilon$ , which remains elevated after a breaking wave for more than one wave period. This means that the strong turbulence generated during breaking has time to be carried through a wide range of fixed  $z$  values, nominally  $-H_s/2 < z < H_s/2$ , before returning to a background level. The effect is to spread the high  $\varepsilon$  values through the surface layer rather than concentrate them exclusively above mean sea level.

The maximum dissipation in the fixed reference frame occurs near the mean sea level ( $z = 0$ ) and decreases both above and below this level (Fig. 2h). Other bursts are similar, and the general result is that the average turbulence accumulates at the average surface. Again, this is because the turbulence persists longer than wave

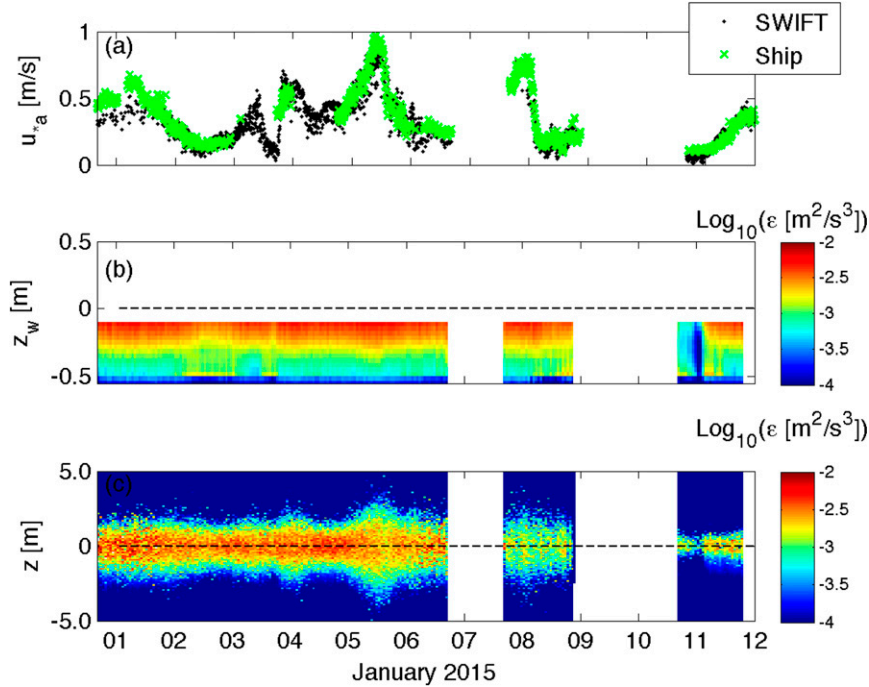


FIG. 3. Time series of processed results (a) wind friction velocity, (b) burst-averaged turbulent dissipation rate in the wave-following reference frame, and (c) burst-averaged turbulent dissipation rate in the fixed reference frame.

phase changes. Above mean sea level, the decrease in the average is caused by assigning zero dissipation when the grid does not have water. Below mean sea level, the decrease in the average is caused by the observed and extrapolated decay of turbulence [Eq. (7)].

### 3. Results

The processed wind and turbulence results are shown in Fig. 3 for a total of 2522 bursts of data, each a burst-averaged ensemble lasting 512 s. Many of these bursts overlap in time because multiple SWIFTs were deployed and collected data simultaneously. The wind friction velocity estimates from the sonic anemometer are consistent with application of a drag coefficient to the SWIFT wind speed measurements; both increase monotonically to approximately  $u_{*a} \approx 1 \text{ m s}^{-1}$  for the max observed wind speed of  $U_{10} = 20 \text{ m s}^{-1}$ . The air-side value  $u_{*a}$  presented in this figure is converted to a water-side value  $u_* = (\rho_a/\rho_w)^{1/2} u_{*a}$  for the remaining presentation of results (i.e., this figure is the only place where  $u_{*a}$  appears).

In Figs. 3b and 3c, the burst-averaged turbulent dissipation rates in the wave-following and fixed reference frames track the time series of wind forcing. The values are generally in the range of  $10^{-4} < \epsilon < 10^{-2} \text{ m}^2 \text{ s}^{-3}$ ,

although some values are as low as  $10^{-5} \text{ m}^2 \text{ s}^{-3}$  during the very calm period on 10 January 2015. The range is consistent with previous observations of the turbulent dissipation rate in the surface layer (e.g., Gemmrich 2010; Schwendeman et al. 2014; Sutherland and Melville 2015). In the wave-following reference frame of Fig. 3b, the dissipation rates are maximum at the surface ( $z_w \sim 0$ ) and decrease with depth. In the fixed reference frame of Fig. 3c, the dissipation rates are maximum at the mean sea level ( $z = 0$ ) and decrease over several meters in depth. This is because the time scales for turbulent dissipation are longer than the time scales of individual waves. As shown in the example of Fig. 2, the turbulence associated with an individual breaking wave persists for more than one wave period. This means the turbulence can be carried from the crest level down to the trough level in  $z$ , even though it may be isolated very near the surface in  $z_w$ . Thus, the time series of  $\epsilon(z)$  in Fig. 3c populate a larger range of the  $z$  grid when the waves are larger.

Figure 3 has scatter in the dissipation rates. The values at the highest wind forcing are mixed with some of the moderate conditions. Some of this can be attributed to the episodic nature of breaking and probability of the number and size of individual breaking waves within each ensemble (a burst-averaged result from 512 s) used

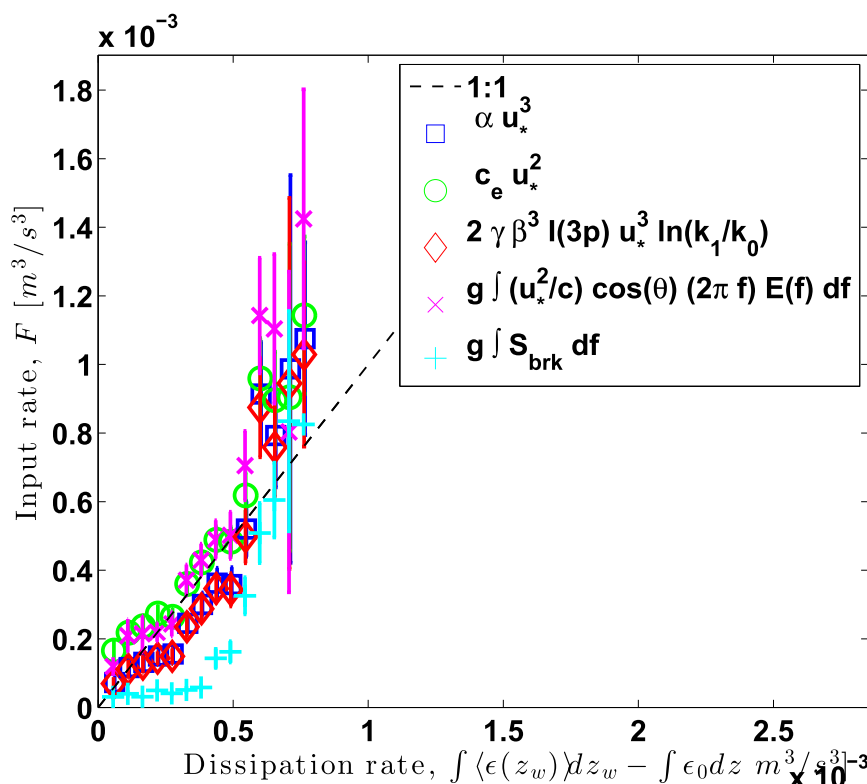


FIG. 4. Integrated rate of energy input from the wind using five different formulations vs measured total turbulence dissipation rate in the upper-ocean surface layer. Symbols show the bin averages and vertical lines show the standard errors.

for SWIFT calculations. Of course, wave dynamics, in addition to wind forcing, control wave breaking, and the combined effects, are evaluated using the various formulations for TKE flux into the ocean surface.

#### a. Integrated (total) energy fluxes

The assumption in most treatments of wave-breaking turbulence is that the input rate of TKE at the ocean surface matches the dissipation rate below the surface [Eq. (1)]. Figure 4 compares the five different estimates for the total TKE input rate  $F$  with the observed turbulence dissipation rates [depth-integrated total in the wave-following reference frame without extrapolation;  $\int \langle \epsilon(z_w) \rangle dz_w$ ] using binned averages. The comparisons are summarized in Table 1, which shows the raw correlation coefficients from all 2522 ensembles (rather than the bin averages). Here, we use a constant  $\alpha = 75$  in  $F_1$  [Eq. (2)] and a constant transfer velocity of  $c_e = 2 \text{ m s}^{-1}$  in  $F_2$  [Eq. (3)]. These were selected as the values within the range from the literature for young seas that give the best comparison with the observations of dissipation. The WAVEWATCH III dissipation values were obtained by integrating  $\int S_{\text{brk}} df$  over frequencies greater than twice the peak frequency. This frequency

integration limit is chosen because swell frequencies have a different dissipation mechanism (Ardhuin et al. 2010).

For the comparison, a background  $\int \langle \epsilon_0 \rangle dz_w = 0.7 \times 10^{-3} \text{ m}^3 \text{ s}^{-3}$  is removed from each ensemble. This is consistent with previous studies (e.g., Thomson et al. 2009; Gemmrich 2010; Schwendeman et al. 2014) where the intent is to isolate the wave-breaking dissipation from dissipation due to shear-driven turbulence (McWilliams et al. 2012), microbreaking (Sutherland and Melville 2015), and swell dissipation (Ardhuin et al. 2010). Here, we have used the wave-resolved estimates

TABLE 1. TKE flux estimates  $F$  and correlation to observed dissipation  $\int \epsilon(z_w) dz_w$ .

Flux estimate	Correlation coefficient $R^2$
$F_1 = \alpha u_*^3$	0.48
$F_2 = c_e u_*^2$	0.53
$F_3 = 2\gamma\beta^3 I(3p) u_*^3 \ln(k_1/k_0)$	0.48
$F_4 = g \int \frac{u_*^2}{c} \cos(\theta) (2\pi f) E(f) df$	0.49
$F_5 = \int S_{\text{brk}} df$	0.52



to dissipation rate to further constrain the determination of the background value. We define background as the median of the lowest half of the values in a given burst (512 s). Note that the dissipation values are highly non-Gaussian because very large values occur episodically during breaking; thus, this definition is not equivalent to the median of the values less than the mean. Using this definition, the background dissipation has almost no variation as a function of wind speed above  $5 \text{ m s}^{-1}$ . The background values are in the range of  $0.5 \times 10^{-3}$  to  $0.9 \times 10^{-3} \text{ m}^3 \text{ s}^{-3}$ , with minimal dependence on wave age or wind speed. Thus, we use a constant  $0.7 \times 10^{-3} \text{ m}^3 \text{ s}^{-3}$  throughout this analysis. Although the definition using the median lowest half of the values may seem an arbitrary choice, this background level is confirmed as the threshold when visible breaking becomes the dominant process, following Gemmrich (2010).

All of the total flux estimates show general agreement with the bin-averaged measurements of turbulent dissipation rate. The formulation using a transfer velocity [ $F_2$  from Eq. (3)] has the best correlation, although the differences among the correlation coefficients are only marginally significant (80% level). The general balance of input and dissipation is consistent with the equilibrium concept of Phillips (1985) and the observations of Thomson et al. (2013), although that study was at lower wind speeds. Similarly, the persistence of a  $f^{-4}$  slope in the wave spectra shown in Schwendeman and Thomson (2015) also suggests equilibrium, following Babanin and Soloviev (1998).

Relative to the in situ dissipation, most of the estimates of the TKE input in Fig. 4 are low during moderate conditions ( $< 0.7 \times 10^{-3} \text{ m}^3 \text{ s}^{-3}$ ) and high during rough conditions ( $> 0.7 \times 10^{-3} \text{ m}^3 \text{ s}^{-3}$ ). The WAVEWATCH III estimates of  $\int S_{\text{brk}} df$  are particularly low during the moderate conditions. This might be related to wave growth during those conditions, although the bulk growth rate is typically less than  $10^{-4} \text{ m}^2 \text{ s}^{-3}$ . The transfer velocity formulation  $F_2$  [Eq. (3)] is the best for matching the in situ dissipation during moderate conditions, but it too exceeds the in situ dissipation values during rough conditions. That all estimates exceed the measurements during rough conditions suggests a process is missing from the data analysis or a deficiency in the observational data itself. It may be that these data simply do not extend deep enough to capture all of the dissipation. Alternatively, bubbles may be important, both to the process of energy dissipation and to the quality of acoustic Doppler data, especially during rough conditions.

Previous results have shown that the work done against the buoyancy of bubbles in breaking waves is additional sink of energy (e.g., Lamarre and Melville

1991). Furthermore, in a competing mechanism, the presence of large bubble clouds near the surface may actually limit surface turbulence in high winds. Deane et al. (2016) suggest that TKE dissipation rates are limited to  $O(10^0) \text{ m}^2 \text{ s}^{-3}$  by the buoyancy stabilization within bubbles clouds and that increasingly energetic wave breaking simply creates larger bubble clouds that achieve this limit. The highest dissipation rates calculated here do not approach the Dean et al. values but that again may be a limitation of the Doppler sonars.

The relationship of bubbles and turbulence is also highlighted by the recent work of Lim et al. (2015), who show that accounting for void fraction is crucial to interpreting the rapid dissipation of wave energy beneath a breaking wave. For the roughest conditions in this dataset ( $20 \text{ m s}^{-1}$  winds), bubbles and “spindrift” (spraying foam) may become important to the total energy flux budget. For spindrift in particular, the transfer of kinetic energy effectively bypasses the waves because energy does not get input to the wave spectrum (where it would be available to dissipate in the breaking process). Restated, the “clipping” off the top of wave crests is a direct transfer of energy on a wave-by-wave basis, as opposed to the indirect transfer described by the equilibrium of wind input and breaking dissipation achieved via the exchanges of many waves in a spectrum.

Bubble dynamics are beyond the scope of this paper, and spray is only beginning to occur at the upper end of this dataset ( $U_{10} = 20 \text{ m s}^{-1}$ ). The pulse-coherent acoustic Doppler methods used on board the SWIFTS are not capable of measuring turbulent velocities inside bubble clouds. The bubble clouds are screened during initial quality control of the raw data, using the pulse correlations and acoustic backscatter, which are reduced and elevated, respectively, by bubbles. Thus, the results herein are confined to the average TKE dissipation rates outside of the bubble clouds. This might significantly change interpretation of the total energy flux balance at the surface. However, the active bubble clouds cover less than 1% of the sea surface at any given time, even at winds of  $> 15 \text{ m s}^{-1}$  (Schwendeman and Thomson 2015), and thus our estimates of the burst-averaged TKE dissipation rate  $\langle \epsilon \rangle$  can be interpreted as values that are characteristic for most of the ocean surface layer. Even though the total dissipation obtained by these methods may be biased low, these characteristic values may be more appropriate when using dissipation as a proxy for gas transfer (Zappa et al. 2007).

### b. Depth scaling

In the wave-following reference frame, the strongest turbulent dissipation rates are isolated to a region very close to the surface ( $z_w > -0.2 \text{ m}$ ), even when the waves

are several meters in height. This is consistent with several published observations (Gemmrich 2010; Thomson 2012; Sutherland and Melville 2015). However, other published observations, using a fixed reference frame, have concluded that strong dissipation occurs much farther below the surface (Terray et al. 1996; Drennan et al. 1996; Feddersen 2012). The apparent contradiction can be reconciled by considering the effect of wave orbital motions in converting the wave-following reference frame to a fixed reference frame using wave-resolved observations. The orbital motions move the surface ( $z = \eta$ ,  $z_w = 0$ ) from crest to trough and back every wave period. While  $z_w = 0$  remains the same, the fixed reference frame  $z$  ranges from  $\eta \approx -H_s/2$  to  $\eta \approx H_s/2$ . If the strong turbulence of a breaking crest persists more than half a wave period, it will be carried down to the trough level  $z = -H_s/2$  while still appearing to be isolated within a shallow region near the surface,  $-0.4 < z_w < 0$  m, as shown in the example of Fig. 2.

Here, the wave-resolved (at 2-s time steps) estimates of dissipation rate are converted using the direct transform  $z = \eta - z_w$  and then burst averaged (at 512-s time steps). The burst-averaged values are denoted with brackets. The burst-averaged profiles in both the  $z_w$  and  $z$  reference frames are then used to evaluate the depth scaling of Eq. (7), which uses significant wave height to normalize a power law decreasing in depth. A single formulation of TKE flux  $F_2$  is used, which is selected based on the quality of correlation in the total dissipation comparison (Table 1). Using other flux estimates has a negligible effect on the resulting depth dependence because the flux estimates are similar over most of the range of the observations.

The depth-scaled results are presented in Fig. 5 and Table 2. In keeping with the original formulation, the scaled results are only presented for depths below mean sea level, and it is important to note that this misses approximately half of the total dissipation. The wave-following  $z_w$  results in decay below the surface and fit a power law with an exponent of approximately  $\lambda \approx 1.4$ . This is consistent with other wave-following observations (Gemmrich 2010; Zippel and Thomson 2015; Thomson et al. 2014) and region 2 of the Terray et al. (1996) observations in a fixed reference frame. The fixed  $z$  results have a similar depth dependence, though shifted deeper, and the exponent is  $\lambda \approx 1.6$ . Both reference frames suggest a region of quasi-constant dissipation near the surface, which was postulated, but not measured, in the fixed frame (Terray et al. 1996, their region 1). In the wave-following frame, the constant region is only 1% of the normalized depth ( $z_w/H_s > -10^{-2}$ ). In the fixed reference frame, the constant region is at least

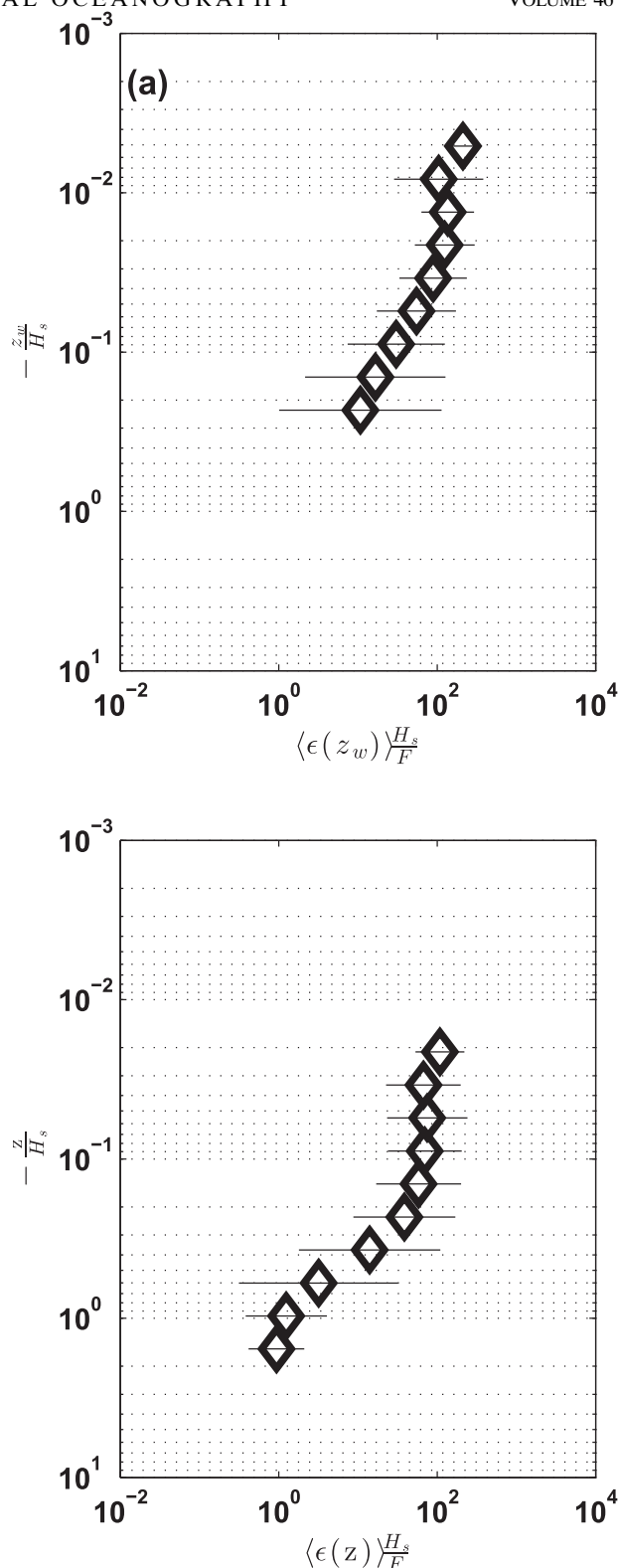


FIG. 5. Scaled vertical profiles of turbulent dissipation rates in (a) the wave-following reference frame and (b) the fixed reference frame. Diamonds show bin averages, and horizontal lines show the standard percent errors (which display symmetrically in logarithm space) at each bin.

TABLE 2. Timescales, reference frames, and scaled results for the measured profiles of TKE dissipation rate  $\varepsilon$ . Confidence intervals on the scaling fits are at 95% significance level.

Dissipation estimate	Time scale	Reference frame	Scaling
$\varepsilon(z_w)$	Phase resolved (2 s)	Wave following ( $z_w = 0$ at sea surface)	N/A
$\varepsilon(z)$	Phase resolved (2 s)	Fixed ( $z = 0$ at mean sea level)	N/A
$\langle \varepsilon(z_w) \rangle$	Burst averaged (512 s)	Wave following ( $z_w = 0$ at sea surface)	$\left(\frac{\overline{\varepsilon} H_s}{F}\right) = \left(\frac{z_w}{H_s}\right)^{-1.41 \pm 0.02}$ for $-\frac{z_w}{H_s} < 10^{-2}$
$\langle \varepsilon(z) \rangle$	Burst averaged (512 s)	( $z = 0$ at mean sea level)	$\left(\frac{\overline{\varepsilon} H_s}{F}\right) = \left(\frac{z}{H_s}\right)^{-1.56 \pm 0.03}$ for $-\frac{z}{H_s} < 10^{-1}$

10% of the normalized depth ( $z/H_s > -10^{-1}$ ). The measurements of the present study do not extend deep enough to observe the third, and deepest, layer discussed in Terray et al. (1996), which is a log layer beneath the wave-affected layer.

Although these results reconcile much of the differences in the literature between fixed reference frames (e.g., Terray et al. 1996) and wave-following reference frames (e.g., Gemmrich 2010), important distinctions remain. Terray et al. (1996) extrapolated dissipations above the trough level [ $z_w/H_s > O(-10^0)$ ] such that the total depth-integrated dissipation matched the TKE input rate  $F$  and the dissipation above the mean sea level was zero. As there are two parameters ( $\varepsilon$  and  $z$ ) and only one hard constraint (matching  $F$ ), there are many other extrapolations that would match  $F$  and yet allow non-zero dissipation above the mean sea level. Revisiting Fig. 7 of Terray et al. (1996), it is clear that the extrapolation is not well constrained because there are only four observations above [ $z_w/H_s > O(-10^0)$ ]. Below their extrapolation, the observations of Terray et al. (1996) are roughly consistent with the observations of the present study.

#### 4. Discussion

In summary, the enhanced turbulence dissipation rates associated with wave breaking are isolated in an extremely shallow surface layer of  $h < 1$  m, yet they also are distributed throughout a thicker, wave-affected layer of  $h < H_s$ . The answer depends on the reference frame. For the purpose of comparing with numerical circulation models, which do not typically include wave-resolved surface waves, the fixed reference frame is commonly used (e.g., Gerbi et al. 2013) and the present results indicate that turbulent dissipation should be included for depths  $h \sim H_s$ . The lingering problem is then what to do with the portion of total dissipation that occurs above mean sea level ( $z > 0$ ). For this dataset, once converted to a fixed reference frame, that portion is approximately half of the total.

The observed quasi-constant layer of dissipation within the upper 10% of the nondimensional fixed reference frame ( $-z/H_s > 10^{-1}$ ) is qualitatively consistent with the recent large-eddy simulation (LES) results of Kukulka and Brunner (2015), and the near-complete dissipation of most wave-breaking energy within the upper few meters is consistent with Noh et al. (2004). Results are also consistent with a diffusive layer below the constant layer (e.g., Craig and Banner 1994; Terray et al. 1996). Results do not extend deep enough to evaluate the expected log-layer below  $-z/H_s < O(10^0)$ . The time scales of the observed dissipation are also qualitatively consistent with numerical studies. Specifically, Sullivan et al. (2004) used direct numerical simulation (DNS) to show that a single breaking wave can energize the surface layer for more than 50 wave periods, and this long time scale is central to the vertical advection of turbulence by orbital motions and phase-resolving change of reference frame presented here.

As to which input TKE flux to use in numerical models, the Gemmrich et al. (1994) effective transfer speed formulation [ $F_2$ ; Eq. (3)] has the best agreement with these observations, although only marginally so. All formulations exceed the observed dissipation at high winds, and this highlights the cubic  $u_*^3$  dependence of  $F_1$  [Eq. (2)]. The Phillips (1985) formulation [ $F_3$ ; Eq. (4)] may be an improvement over the simpler  $u_*^3$ , but it is important to note that  $F_3$  here is really just  $u_*^3$  with a different coefficient, since the ratio  $\ln(k_1/k_0)$  is fixed at  $\ln(2.5)$  with our definition of the equilibrium range as  $k_0 < k_m < k_1$ . If, instead, the  $k_1 = gu_*^{-2}$  prescription from Phillips (1985) is used, the total TKE input rate does indeed have a dependence less steep than  $u_*^3$ . This alternate form has a negligible effect in comparing to this dataset; however, the subtleties of the Phillips (1985) formulation may be useful in future studies.

Assuming a total energy balance [Eq. (1)] for every burst-averaged ensemble (2522 total), effective transfer speeds can be estimated rather than prescribed as the

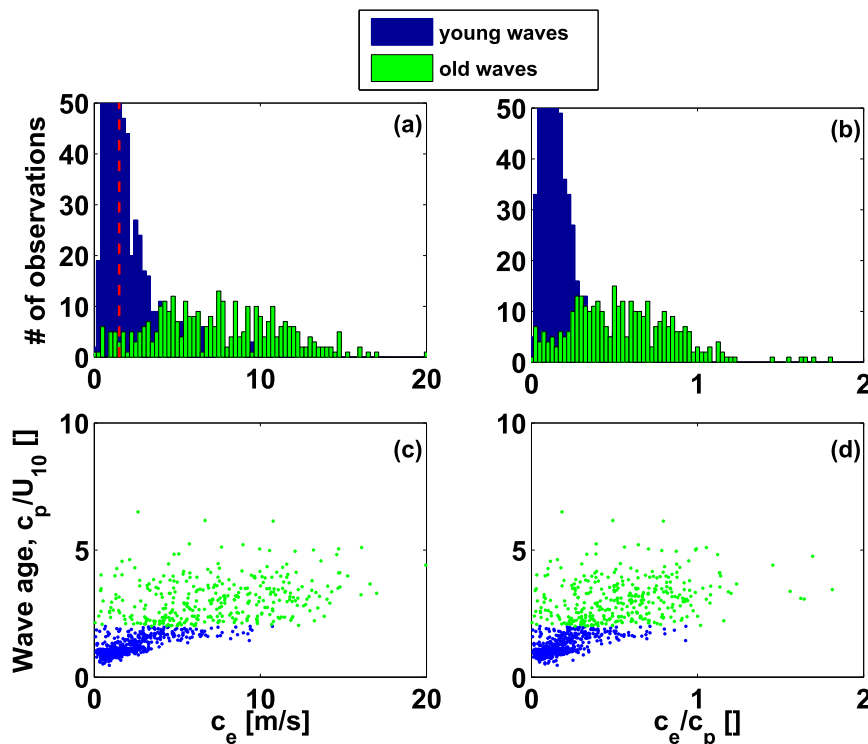


FIG. 6. Empirical transfer velocities  $c_e$  as (a),(b) histograms and (c),(d) correlated with wave age. Values are (left) dimensional and (right) scaled by peak wave phase speed. Young waves (wave age < 2) are shown in blue. Mature seas (wave age > 2) are shown in green. The constant  $c_e = 2 \text{ m s}^{-1}$  used in the earlier sections is shown as a red line in (a).

constant  $c_e = 2 \text{ m s}^{-1}$  used in the preceding sections. Figure 6 shows these empirical transfer speeds in histograms, and versus wave age, as dimensional and non-dimensional (normalized by peak wave phase speed) values. The dimensional histograms are consistent with the  $2 \text{ m s}^{-1}$  value taken as a constant in the preceding analysis. This also is consistent with the concept of short waves, which travel slowly, providing the roughness elements upon which the wind stress can do work (i.e., transfer energy).

The values in Fig. 6 are separated into young seas (blue points) and mature seas (green points) using the wave age (ratio of the peak wave phase speed  $c_p$  to the wind speed  $U_{10}$ ). For young seas, the equilibrium input-dissipation balance works well, and the histogram is centered on  $c_e = 2 \text{ m s}^{-1}$  as expected. When normalized by the peak phase speed, the histogram is centered on  $c_e/c_p = 1/5$ . For mature seas, the equilibrium balance is not a valid assumption because dissipation is likely to exceed input. Figure 6 shows the spuriously high  $c_e$  values that result in order to match large dissipations with smaller inputs if the equilibrium calculation is applied to mature seas. The effect is most severe at large wave ages. The clear recommendation is to restrict

application of the effective transfer velocity formulation to young seas.

## 5. Conclusions

In situ observations of turbulent dissipation rates immediately below the wave-following surface of the ocean are consistent with several estimates for the input of TKE by a wind stress performing work on a wave surface. A formulation using an effective transfer speed associated with the short waves gives the best match to the data, although all formulations give reasonable results. Wave-resolved conversion of the wave-following measurements to a fixed reference frame show that the depth penetration of the turbulence is strongly affected by wave orbital motions, such that turbulence can be carried down to the trough level and below (relative to mean sea level). The depth dependence can be modeled as a power-law decay scaled by wave height.

*Acknowledgments.* Joe Talbert, Alex de Klerk, Adam Brown, and Jarett Goldsmith assisted in all aspects of data collection, including development and improvements for the SWIFT platform. The captain and crew of

the R/V *T. G. Thompson* provide excellent logistical and deployment support. Eric D'Asaro provided many helpful comments on the manuscript, as did two anonymous reviewers. Funding for JT, MS, and SZ was provided by the National Science Foundation (OCE-1332719). Funding for ER was provided by the Office of Naval Research through an NRL Core Project (Program Element 0602435N). The SWIFT wave, wind, and turbulence data are available online (at [www.apl.uw.edu/swift](http://www.apl.uw.edu/swift)) by serial number. The waverider spectra are available as station 166 from the Coastal Data Information Program (CDIP) at the Scripps Institution of Oceanography or the National Data Buoy Center (NDBC) as station 46246.

## REFERENCES

- Agrawal, Y. C., E. A. Terray, M. A. Donelan, P. A. Hwang, A. J. Williams III, W. M. Drennan, K. K. Kahma, and S. A. Kitaigorodskii, 1992: Enhanced dissipation of kinetic energy beneath surface waves. *Nature*, **359**, 219–220, doi:[10.1038/359219a0](https://doi.org/10.1038/359219a0).
- Ardhuin, F., and Coauthors, 2010: Semiempirical dissipation source functions for ocean waves. Part I: Definitions, calibration, and validations. *J. Phys. Oceanogr.*, **40**, 1917–1941, doi:[10.1175/2010JPO4324.1](https://doi.org/10.1175/2010JPO4324.1).
- Babanin, A. V., and Y. P. Soloviev, 1998: Field investigation of transformation of wind wave frequency spectrum with fetch and stage of development. *J. Phys. Oceanogr.*, **28**, 563–576, doi:[10.1175/1520-0485\(1998\)028<0563:FIOTOT>2.0.CO;2](https://doi.org/10.1175/1520-0485(1998)028<0563:FIOTOT>2.0.CO;2).
- Banner, M., J. Gemmrich, and D. Farmer, 2002: Multiscale measurements of ocean wave breaking probability. *J. Phys. Oceanogr.*, **32**, 3364–3375, doi:[10.1175/1520-0485\(2002\)032<3364:MMOOWB>2.0.CO;2](https://doi.org/10.1175/1520-0485(2002)032<3364:MMOOWB>2.0.CO;2).
- Burchard, H., and Coauthors, 2008: Observational and numerical modeling methods for quantifying coastal ocean turbulence and mixing. *Prog. Oceanogr.*, **76**, 399–442, doi:[10.1016/j.pocean.2007.09.005](https://doi.org/10.1016/j.pocean.2007.09.005).
- Craig, P. D., and M. L. Banner, 1994: Modeling wave-enhanced turbulence in the ocean surface layer. *J. Phys. Oceanogr.*, **24**, 2546–2559, doi:[10.1175/1520-0485\(1994\)024<2546:MWETIT>2.0.CO;2](https://doi.org/10.1175/1520-0485(1994)024<2546:MWETIT>2.0.CO;2).
- Deane, G. B., M. D. Stokes, and A. H. Callaghan, 2016: The saturation of fluid turbulence in breaking laboratory waves and implications for whitecaps. *J. Phys. Oceanogr.*, **46**, 975–992, doi:[10.1175/JPO-D-14-0187.1](https://doi.org/10.1175/JPO-D-14-0187.1).
- Drennan, W. M., M. A. Donelan, E. A. Terray, and K. B. Katsaros, 1996: Oceanic turbulence dissipation measurements during SWADE. *J. Phys. Oceanogr.*, **26**, 808–815, doi:[10.1175/1520-0485\(1996\)026<0808:OTDMIS>2.0.CO;2](https://doi.org/10.1175/1520-0485(1996)026<0808:OTDMIS>2.0.CO;2).
- Feddersen, F., 2012: Observations of the surfzone turbulent dissipation rate. *J. Phys. Oceanogr.*, **42**, 386–399, doi:[10.1175/JPO-D-11-082.1](https://doi.org/10.1175/JPO-D-11-082.1).
- Gemmrich, J., 2010: Strong turbulence in the wave crest region. *J. Phys. Oceanogr.*, **40**, 583–595, doi:[10.1175/2009JPO4179.1](https://doi.org/10.1175/2009JPO4179.1).
- , and D. Farmer, 2004: Near-surface turbulence in the presence of breaking waves. *J. Phys. Oceanogr.*, **34**, 1067–1086, doi:[10.1175/1520-0485\(2004\)034<1067:NTITPO>2.0.CO;2](https://doi.org/10.1175/1520-0485(2004)034<1067:NTITPO>2.0.CO;2).
- , T. Mudge, and V. Polonichko, 1994: On the energy input from wind to surface waves. *J. Phys. Oceanogr.*, **24**, 2413–2417, doi:[10.1175/1520-0485\(1994\)024<2413:OTEIFW>2.0.CO;2](https://doi.org/10.1175/1520-0485(1994)024<2413:OTEIFW>2.0.CO;2).
- Gerbi, G. P., R. J. Chant, and J. L. Wilkin, 2013: Breaking surface wave effects on river plume dynamics during upwelling-favorable winds. *J. Phys. Oceanogr.*, **43**, 1959–1980, doi:[10.1175/JPO-D-12-0185.1](https://doi.org/10.1175/JPO-D-12-0185.1).
- Goring, D. G., and V. I. Nikora, 2002: Despiking acoustic Doppler velocimeter data. *J. Hydraul. Eng.*, **128**, 117–126, doi:[10.1061/\(ASCE\)0733-9429\(2002\)128:1\(117\)](https://doi.org/10.1061/(ASCE)0733-9429(2002)128:1(117)).
- Govender, K., G. P. Mocke, and M. J. Alport, 2004: Dissipation of isotropic turbulence and length-scale measurements through the wave roller in laboratory spilling waves. *J. Geophys. Res.*, **109**, C08018, doi:[10.1029/2003JC002233](https://doi.org/10.1029/2003JC002233).
- Herbers, T. H. C., P. F. Jessen, T. T. Janssen, D. B. Colbert, and J. H. MacMahan, 2012: Observing ocean surface waves with GPS-tracked buoys. *J. Atmos. Oceanic Technol.*, **29**, 944–959, doi:[10.1175/JTECH-D-11-00128.1](https://doi.org/10.1175/JTECH-D-11-00128.1).
- Hogan, T., and Coauthors, 2014: The navy global environmental model. *Oceanography*, **27**, 116–125, doi:[10.5670/oceanog.2014.73](https://doi.org/10.5670/oceanog.2014.73).
- Hwang, P. A., F. J. Ocampo-Torres, and H. García-Nava, 2012: Wind sea and swell separation of 1D wave spectrum by a spectrum integration method. *J. Atmos. Oceanic Technol.*, **29**, 116–128, doi:[10.1175/JTECH-D-11-00075.1](https://doi.org/10.1175/JTECH-D-11-00075.1).
- Kitaigorodskii, S. A., 1983: On the theory of the equilibrium range in the spectrum of wind-generated gravity waves. *J. Phys. Oceanogr.*, **13**, 816–827, doi:[10.1175/1520-0485\(1983\)013<0816:OTTOTE>2.0.CO;2](https://doi.org/10.1175/1520-0485(1983)013<0816:OTTOTE>2.0.CO;2).
- Kolmogorov, A. N., 1941: Dissipation of energy in the locally isotropic turbulence. *Dokl. Akad. Nauk SSR*, **30**, 301–305.
- Kukulka, T., and K. Brunner, 2015: Passive buoyant tracers in the ocean surface boundary layer: 1. Influence of equilibrium wind-waves on vertical distributions. *J. Geophys. Res. Oceans*, **120**, 3837–3858, doi:[10.1002/2014JC010487](https://doi.org/10.1002/2014JC010487).
- Lamarre, E., and W. Melville, 1991: Air entrainment and dissipation in breaking waves. *Nature*, **351**, 469–472, doi:[10.1038/351469a0](https://doi.org/10.1038/351469a0).
- Lim, H.-J., K.-A. Chang, Z.-C. Huang, and B. Na, 2015: Experimental study on plunging breaking waves in deep water. *J. Geophys. Res. Oceans*, **120**, 2007–2049, doi:[10.1002/2014JC010269](https://doi.org/10.1002/2014JC010269).
- McWilliams, J. C., E. Huckle, J.-H. Liang, and P. P. Sullivan, 2012: The wavy Ekman layer: Langmuir circulations, breaking waves, and Reynolds stress. *J. Phys. Oceanogr.*, **42**, 1793–1816, doi:[10.1175/JPO-D-12-07.1](https://doi.org/10.1175/JPO-D-12-07.1).
- Melville, W. K., 1994: Energy dissipation by breaking waves. *J. Phys. Oceanogr.*, **24**, 2041–2049, doi:[10.1175/1520-0485\(1994\)024<2041:EDBBW>2.0.CO;2](https://doi.org/10.1175/1520-0485(1994)024<2041:EDBBW>2.0.CO;2).
- Noh, Y., H. S. Min, and S. Raasch, 2004: Large eddy simulation of the ocean mixed layer: The effects of wave breaking and Langmuir circulation. *J. Phys. Oceanogr.*, **34**, 720–735, doi:[10.1175/1520-0485\(2004\)034<0720:LESOTO>2.0.CO;2](https://doi.org/10.1175/1520-0485(2004)034<0720:LESOTO>2.0.CO;2).
- Phillips, O. M., 1985: Spectral and statistical properties of the equilibrium range in wind-generated gravity waves. *J. Fluid Mech.*, **156**, 505–531, doi:[10.1017/S0022112085002221](https://doi.org/10.1017/S0022112085002221).
- Plant, B., 1982: A relationship between wind stress and wave slope. *J. Geophys. Res.*, **87**, 1961–1967, doi:[10.1029/JC087iC03p01961](https://doi.org/10.1029/JC087iC03p01961).
- Schwendeman, M., and J. Thomson, 2015: Observations of white-cap coverage and the relation to wind stress, wave slope, and turbulent dissipation. *J. Geophys. Res. Oceans*, **120**, 8346–8363, doi:[10.1002/2015JC011196](https://doi.org/10.1002/2015JC011196).
- , —, and J. Gemmrich, 2014: Wave breaking dissipation in a young wind sea. *J. Phys. Oceanogr.*, **44**, 104–127, doi:[10.1175/JPO-D-12-0237.1](https://doi.org/10.1175/JPO-D-12-0237.1).



- Smith, S. D., 1988: Coefficients for sea surface wind stress, heat flux, and wind profiles as a function of wind speed and temperature. *J. Geophys. Res.*, **93**, 15 467–15 472, doi:[10.1029/JC093iC12p15467](https://doi.org/10.1029/JC093iC12p15467).
- Sullivan, P. P., J. C. McWilliams, and W. K. Melville, 2004: The oceanic boundary layer driven by wave breaking with stochastic variability. Part 1. Direct numerical simulations. *J. Fluid Mech.*, **507**, 143–174, doi:[10.1017/S0022112004008882](https://doi.org/10.1017/S0022112004008882).
- Sutherland, P., and W. K. Melville, 2015: Field measurements of surface and near-surface turbulence in the presence of breaking waves. *J. Phys. Oceanogr.*, **45**, 943–965, doi:[10.1175/JPO-D-14-0133.1](https://doi.org/10.1175/JPO-D-14-0133.1).
- Terray, E., M. Donelan, Y. Agrawal, W. Drennan, K. Kahma, A. Williams, P. Hwang, and S. Kitaigorodskii, 1996: Estimates of kinetic energy dissipation under breaking waves. *J. Phys. Oceanogr.*, **26**, 792–807, doi:[10.1175/1520-0485\(1996\)026<0792:EOKEDU>2.0.CO;2](https://doi.org/10.1175/1520-0485(1996)026<0792:EOKEDU>2.0.CO;2).
- Thomson, J., 2012: Wave breaking dissipation observed with SWIFT drifters. *J. Atmos. Oceanic Technol.*, **29**, 1866–1882, doi:[10.1175/JTECH-D-12-00018.1](https://doi.org/10.1175/JTECH-D-12-00018.1).
- , J. R. Gemmrich, and A. T. Jessup, 2009: Energy dissipation and the spectral distribution of whitecaps. *Geophys. Res. Lett.*, **36**, L11601, doi:[10.1029/2009GL038201](https://doi.org/10.1029/2009GL038201).
- , E. A. D’Asaro, M. Cronin, E. Rogers, R. Harcourt, and A. Scherbina, 2013: Waves and the equilibrium range at Ocean Weather Station P. *J. Geophys. Res. Oceans*, **118**, 5951–5962, doi:[10.1002/2013JC008837](https://doi.org/10.1002/2013JC008837).
- , A. R. Horner-Devine, S. Zippel, C. Rusch, and W. Geyer, 2014: Wave breaking turbulence at the offshore front of the Columbia River plume. *Geophys. Res. Lett.*, **41**, 8987–8993, doi:[10.1002/2014GL062274](https://doi.org/10.1002/2014GL062274).
- Tolman, H. L., 1991: A third-generation model for wind waves on slowly varying, unsteady, and inhomogeneous depths and currents. *J. Phys. Oceanogr.*, **21**, 782–797, doi:[10.1175/1520-0485\(1991\)021<0782:ATGMFW>2.0.CO;2](https://doi.org/10.1175/1520-0485(1991)021<0782:ATGMFW>2.0.CO;2).
- , and D. Chalikov, 1996: Source terms in a third-generation wind wave model. *J. Phys. Oceanogr.*, **26**, 2497–2518, doi:[10.1175/1520-0485\(1996\)026<2497:STIATG>2.0.CO;2](https://doi.org/10.1175/1520-0485(1996)026<2497:STIATG>2.0.CO;2).
- , and Coauthors, 2014: User manual and system documentation of WAVEWATCH III version 4.18. NOAA/NWS/NCEP/MMAB Tech. Note 316, 282 pp.
- Wiles, P., T. P. Rippeth, J. Simpson, and P. Hendricks, 2006: A novel technique for measuring the rate of turbulent dissipation in the marine environment. *Geophys. Res. Lett.*, **33**, L21608, doi:[10.1029/2006GL027050](https://doi.org/10.1029/2006GL027050).
- Yelland, M., P. Taylor, I. Consterdine, and M. Smith, 1994: The use of the inertial dissipation technique for shipboard wind stress determination. *J. Atmos. Oceanic Technol.*, **11**, 1093–1108, doi:[10.1175/1520-0426\(1994\)011<1093:TUOTID>2.0.CO;2](https://doi.org/10.1175/1520-0426(1994)011<1093:TUOTID>2.0.CO;2).
- Zappa, C. J., W. R. McGillis, P. A. Raymond, J. B. Edson, E. J. Hints, H. J. Zemmelen, J. W. H. Dacey, and D. T. Ho, 2007: Environmental turbulent mixing controls on air-water gas exchange in marine and aquatic systems. *Geophys. Res. Lett.*, **34**, L10601, doi:[10.1029/2006GL028790](https://doi.org/10.1029/2006GL028790).
- Zippel, S., and J. Thomson, 2015: Wave breaking and turbulence at a tidal inlet. *J. Geophys. Res. Oceans*, **120**, 1016–1031, doi:[10.1002/2014JC010025](https://doi.org/10.1002/2014JC010025).